Journal of Power Sources 196 (2011) 5555–5563

Contents lists available at ScienceDirect

Journal of Power Sources

journal homepage: www.elsevier.com/locate/jpowsour

Closed-loop hydration dynamics in the membrane of a PEM fuel cell

Syed K. Ahmed, Donald J. Chmielewski*

Center for Electrochemical Science & Engineering, Department of Chemical & Biological Engineering, Illinois Institute of Technology, Chicago, IL 60616, United States

ARTICLE INFO

Article history:
Received 3 January 2011
Accepted 28 January 2011
Available online 21 March 2011

Keywords:
Fuel cell
Dynamic simulation
Electrochemistry
Membranes
Process control
Transient response

ABSTRACT

Water management has long been recognized as a critical issue in the operation of a Polymer Electrolyte Membrane Fuel Cell (PEMFC). If the membrane is allowed to dehydrate then ionic conductivity will drop and result in significant power losses. At the opposite extreme, if not enough water is removed from the membrane then liquid water will accumulate in the Gas Diffusion Layer (GDL) and block the transport of reactants to the reaction sites. In this work, the dynamics of membrane hydration are analyzed while under the influence of a closed-loop control system. From a controller assessment perspective, the membrane model is unique in that through the plane spacially dependent water accumulation is captured. By combining with an electrochemical model and simple material and energy balances over the solid and fluid materials, the dynamics of the membrane are shown to be strongly influenced by the thermal responses of the solid as well as humidity levels in the gas streams, all of which are a function of the controller utilized. We conclude by illustrating the highly sensitive nature of the system with respect to water diffusivity within the membrane.

1. Introduction

The objective of a Polymer Electrolyte Membrane Fuel Cell (PEMFC) is to convert hydrogen into electric power. Central to PEMFC efficiency is the ionic conductivity of the membrane, which is strongly influenced by membrane hydration levels. Specifically, greater hydration will result in greater conductivity and thus a more efficient cell. However, if hydration levels exceed the capacity of the membrane, then a layer of liquid water will begin to form and block the transfer of reactants to the reaction sites. Thus, the operational objective with regard to membrane hydration is to operate at a level just below the flooding limit. Unfortunately, the anticipated applications of a PEMFC (most notably automotive) suggest that frequent changes in power demand will be the norm. Since the reaction product is water, rate changes in power demand will result in changes in water production within the membrane.

From a steady-state perspective, the water management challenge is to ensure that water removal rates are equal to production. While water production is proportional to current density, the flux of water from the membrane is a complicated function of operating temperature and hydration level (within the membrane as well as within the reactant gases). Within the dynamic framework, there is the additional question of hydration level excursions during transient periods. In some cases, the system may not recover from an excursion into flooding or dehydration, even if a steady-state based analysis suggests otherwise. Within these transient scenarios key factors include the hydration capacity of the membrane and the flowing gases as well as thermal response time.

Due to the diversity of phenomena occurring within a rather complex structure, a wide variety of PEMFC models can be developed, each focusing on a different dimension and time/length scale. Overviews of PEMFC modeling can be found in [1–4]. In the following we will focus on models of the membrane. Initial efforts to model the membrane in a PEMFC include Springer et al. [5] and Bernardi and Verbrugge [6]. Concerning flux of water through the membrane both include the electro-osmotic drag term, which is proportional to current density and causes water to move toward the cathode. In the Springer et al. [5] model, the flux also includes a back diffusion term, which serves to counter act the impact of electro-osmotic drag. In the Bernardi and Verbrugge model, a hydraulic pressure term is used to counteract electro-osmotic drag. Efforts that directly employ the Bernardi and Verbrugge membrane model include Eikerling et al. [7] and Baschuk and Li [8]. The work of Springer et al. [5] also proposed hydration dependent relationships for the electro-osmotic drag coefficient, the diffusion coefficient and the ionic conductivity of the membrane.

Nguyen and White [9] extended the one-dimensional (through the membrane) model of [5] to include an along the channel dimension. However, to reduce model complexity the differential aspects of the through the membrane direction were approximated by algebraic relations. Specifically, diffusion flux became a function of the hydration difference between cathode and anode, and ionic conductivity became a function of the hydration average between anode and cathode. The effort by Yi and Nguyen [10] extended the

* Corresponding author. Tel.: +1 312 567 3537; fax: +1 312 567 8874.
E-mail address: chmielewski@iit.edu (D.J. Chmielewski).

0378-7753/$ – see front matter © 2011 Elsevier B.V. All rights reserved.
doi:10.1016/j.jpowsour.2011.01.096

Nomenclature

Super- and sub-scripts

a, *c*, *j*, *e*, *s*, *m*	anode, cathode, jacket, ambient, solids, membrane
J	flux (mol cm^{-2} s^{-1})
C	concentration (mol cm^{-3})
T	temperature (K)
F	volumetric flow (cm^3 s^{-1})
r	reaction rate
j	current density (A cm^{-2})
E	voltage (V)
$\mathcal{R}$	resistance of membrane (Ωcm^2)
σ	conductivity in membrane (S/m^2)
P_e	power density (W cm^{-2})
a_w	activity of water in the membrane
P	Partial pressure (atm)

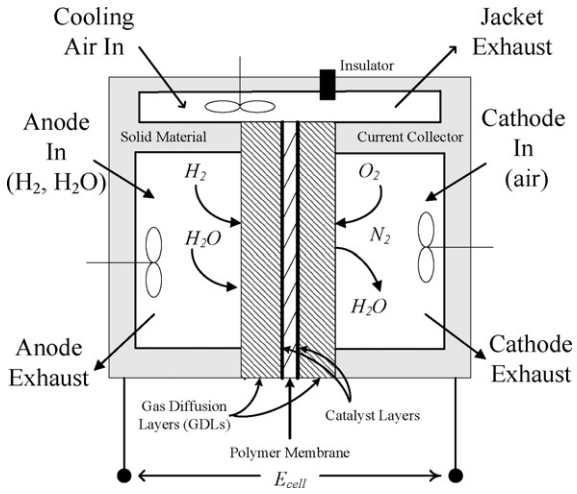

Fig. 1. Schematic of the PEMFC system.

model of [9] by including the hydraulic pressure term (of Bernardi and Verbrugge [6]) in the water flux expression. Again the differential aspect of the through the membrane direction was replaced by algebraic relations. Efforts that employ the Yi and Nguyen [10] approach include Rowe and Li [11], Wu et al. [12], and Zhou et al. [13]. In You and Liu [14] the membrane model and cell configuration of Yi and Nguyen [10] is revisited, but the differential aspects of the through the membrane direction are retained and solved via a Computation Fluid Dynamics (CFD) approach.

All of the models discussed up to this point have been of the steady-state variety. The first class of dynamic models is those that place dynamic descriptions of temperature and gas composition on top of a steady-state model of the membrane. For the most part, papers in this class assume algebraic relations for the through the plane direction and view the cell as being a single lump (Pukrushpan et al. [15], Lauzze and Chmielewski [16], and Zhang et al. [17]) or as having an along the channel spacial direction (Golbert and Lewin [18,19] and Methekar et al. [20]). In De Francesco and Arate [21] a differential perspective is used in the through the plane direction while a single lump is employed for the along the channel direction.

The second class of dynamic models are those that try to capture the membrane's ability to store water and quantify the time rate of change of this stored water. In Shan and Choe [22] the entire membrane is considered a single lump and water flux terms at the anode and cathode sides are used to quantify the accumulation of water. In Chia et al. [23], a similar single lump configuration is used, and then extended to a lumps in series configuration to approximate the along the channel spacial direction. In Chen et al. [24], water accumulation in the through the plane direction is quantified. In Wang and Wang [25] and Um and Wang [26], CFD methods are used to simulate water accumulation in both the through the plane direction and the along the channel direction.

Concerning experimental studies of membrane hydration, Bellows et al. [27], have used neutron imagining methods to measure hydration profiles in the through the plane direction. Unfortunately, limitations in measurement fidelity have made it challenging to characterize hydration dynamics in the through the plane direction [28,29].

The objective of this paper is to develop an accumulation based through the plane membrane model, similar to those of [24–26], but then analyze this model within a closed-loop perspective. As illustrated by the above literature review, closed-loop analysis of an accumulation type model seems to be missing from the PEMFC modeling as well as the PEMFC control literature. The current effort aims to fill this gap.

The paper is organized as follows. The PEMFC model is presented in Section 2, and it is solutions procedure is discussed in Section 3. Analysis of the model under a variety of closed-loop control configurations is given in Section 4. Section 5 presents some additional discussion concerning the topics of flooding and diffusion within the membrane.

2. PEMFC model

The system scenario is similar to that of Lauzze and Chmielewski [16]. From a global perspective the PEMFC stack is assumed to be of sufficient size that air cooling is required (approximately 10 kW$_e$). However, the model presented reflects the volume and surface areas of a single flow channel, under the assumption that macroscopic stack values for power, current, and flow rate can be obtained by appropriate multiplication of this modeling unit. Additionally, the spacial aspect of the single flow channel will be ignored in favor of the simplicity of a Continuous Stirred Tank Reactor (CSTR) form. In spite of this neglect of along the channel spacial dependance, we have found this model to exhibit sufficient richness. In contrast to [16], the new model considers an open-ended humidified hydrogen feed and of course hydration dynamics within the membrane.

The unit cell of the model consist of two gas chambers separated by a membrane electrode assembly (MEA), see Fig. 1. On the anode side, hydrogen is split into hydrogen ions and electrons. While the ions travel through the membrane, the electrons travel through the catalyst layer and the Gas Diffusion Layer (GDL) to the current collector and on to the load. These electrons then travel back to the cathode where they combine with the hydrogen ions and oxygen to produce water. The rate of reaction is proportional to the current density $j/n\mathcal{F} = -r_{\mathrm{H}_2} = -1/2 r_{\mathrm{O}_2} = r_{\mathrm{H}_2\mathrm{O}}$ where r_i represents the generation of species i per unit area of membrane. While the membrane is designed to be impermeable to H_2 and O_2, it is capable of significant water uptake. As such r_{H_2O} cannot be used for the gas phase material balances. Instead, a pair of water transfer fluxes to the membrane from the anode and cathode gas chambers, $J^a_{\mathrm{H}_2\mathrm{O}}$ and $J^c_{\mathrm{H}_2\mathrm{O}}$, will be defined.

While flowrate through the cathode is a good heat removal mechanism, it is common to augment the system with a cooling jacket, the third chamber of Fig. 1. On the subject of heat transfer, the surface area for heat transfer in the cathode and anode chambers is more than just the membrane surface area, A_m. Specifically, the current collector flow channel walls that surround the gas chambers are also available for heat transfer. As such, we assume all of this solid material including the membrane to be a single lump for

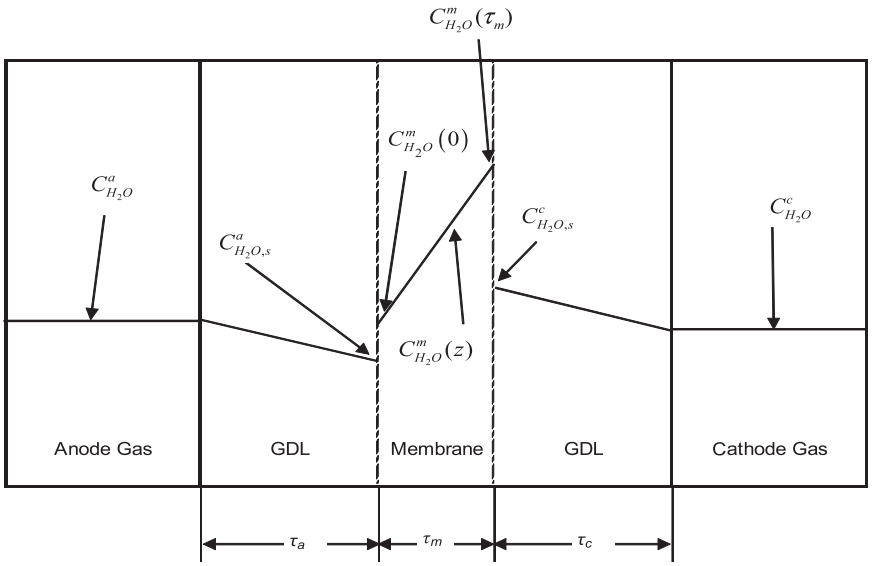

Fig. 2. Schematic of water concentration profiles.

energy balance purposes. Finally, heat transfer can also occur with the environment, specifically losses from the stack edges. Thus, an effective surface area is assumed based on the expected ratio of insulated surface area to the stack volume, and then applied to the volume of the unit cell.

2.1. Material and energy balances

Using the above description, the following material and energy balances are developed. In the anode chamber:

$$V_a \frac{dC^a_{\mathrm{H_2}}}{dt} = F^a_o C^a_{\mathrm{H_2},o} - F^a_1 C^a_{\mathrm{H_2}} + r_{\mathrm{H_2}} A_m \tag{1}$$

$$V_a \frac{dC^a_{\mathrm{H_2O}}}{dt} = F^a_o C^a_{\mathrm{H_2O},o} - F^a_1 C^a_{\mathrm{H_2O}} - J^a_{\mathrm{H_2O}} A_m \tag{2}$$

$$V_a \frac{dT^a}{dt} = \frac{F^a_o T^a_o - F^a_1 T^a + ((UA)_a / C_{ig}\tilde{C}_{p,ig})(T^s - T^a) + (r_{\mathrm{H_2}} T^a - J^a_{\mathrm{H_2O}} T^a) A_m}{C_{ig}} \tag{3}$$

$$F^a_1 = \frac{F^a_o + (r_{\mathrm{H_2}} - J^a_{\mathrm{H_2O}}) A_m}{C_{ig}} \tag{4}$$

In the cathode chamber:

$$V_c \frac{dC^c_{\mathrm{O_2}}}{dt} = F^c_o C^c_{\mathrm{O_2},o} - F^c_1 C^c_{\mathrm{O_2}} + r_{\mathrm{O_2}} A_m \tag{5}$$

$$V_c \frac{dC^c_{\mathrm{H_2O}}}{dt} = F^c_o C^c_{\mathrm{H_2O},o} - F^c_1 C^c_{\mathrm{H_2O}} - J^c_{\mathrm{H_2O}} A_m \tag{6}$$

$$V_c \frac{dT^c}{dt} = \frac{F^c_o T^c_o - F^c_1 T^c + ((UA)_c / C_{ig}\tilde{C}_{p,ig})(T^s - T^c) + (r_{\mathrm{O_2}} T^c - J^c_{\mathrm{H_2O}} T^c) A_m}{C_{ig}} \tag{7}$$

$$F^c_1 = \frac{F^c_o + (r_{\mathrm{O_2}} - J^c_{\mathrm{H_2O}}) A_m}{C_{ig}} \tag{8}$$

At the solid material and cooling jacket:

$$V_j \frac{dT^j}{dt} = F^j T^j_o - F^j T^j + \frac{(UA)_j}{(\rho C_p)_j}(T^s - T^j) \tag{9}$$

$$\begin{aligned}(\rho\tilde{C}_p)_s V_s \frac{dT^s}{dt} &= (UA)_a(T^a - T^s) + (UA)_c(T^c - T^s) + (UA)_j(T^j - T^s) \\ &\quad + (UA)_e(T^e - T^s) - (r_{\mathrm{H_2}} T^a + r_{\mathrm{O_2}} T^c - J^a_{\mathrm{H_2O}} T^a \\ &\quad - J^c_{\mathrm{H_2O}} T^c) A_m \tilde{C}_{p,ig} + Q_{gen} A_m\end{aligned} \tag{10}$$

The heat generation term Q_{gen} is the amount of heat produced by the electrochemical reaction, given by $Q_{gen} = (\Delta H_{f,\mathrm{H_2O}}) r_{\mathrm{H_2O}} - P_e$, where $P_e = jE_{cell}$. It is additionally noted that the above balances assume positive values for $J^a_{\mathrm{H_2O}}$ and $J^c_{\mathrm{H_2O}}$. If either flux is negative then the appropriate terms are replaced by $J^a_{\mathrm{H_2O}} T^s$ or $J^c_{\mathrm{H_2O}} T^s$ in (3), (7) and (10).

2.2. Electrochemical model

The cell voltage is the ideal minus losses

$$E_{cell} = E_{ner} - E_{act} - E_{ohm} - E_{mt} \tag{11}$$

$E_{ner} = E^o + (RT^{(s)}/n\mathcal{F}) \ln(P_{\mathrm{H_2}} P^{1/2}_{\mathrm{O_2}} / P_{\mathrm{H_2O}})$ is the Nernst potential. The activation loss is $E_{act} = (1/\alpha)(RT^{(s)}/n\mathcal{F}) \ln(j/j_o)$, where j_o is the exchange current density. The ohmic loss is $E_{ohm} = j\mathcal{R}$, where $\mathcal{R} = \int_0^{\tau_m} dz/\sigma(z)$, $\sigma(z) = 0.005193\lambda(z) - 0.00326\exp(1269.0(1/303 - 1/T))$, $\lambda(z) = C^m_{\mathrm{H_2O}}(z)/N_s$ and $C^m_{\mathrm{H_2O}}(z)$ is the hydration level within the membrane (defined in the next sub-section). The membrane thickness is τ_m ($z = 0$ is anode side and $z = \tau_m$ is the cathode side). The mass transfer loss is $E_{mt} = \left(1/2 + 1/\alpha\right)(RT^{(s)}/n\mathcal{F}) \ln(j_L/(j_L - j))$, where $j_L = 2n\mathcal{F}k^c_{gdl} C^c_{\mathrm{O_2}}$ is the limiting current density. The mass transfer coefficient across the GDL is $k^i_{gdl} = D^i_{gdl}/\tau_i$ where τ_i is the thickness and D^i_{gdl} is the diffusivity of the GDL ($i = a$ or c).

2.3. Membrane hydration model

A water balance within the membrane yields:

$$\frac{\partial C^m_{\mathrm{H_2O}}}{\partial t} = -\frac{\partial J^m_{\mathrm{H_2O}}}{\partial z} \tag{12}$$

where $C^m_{\mathrm{H_2O}}$ is the concentration of water in the membrane and $J^m_{\mathrm{H_2O}}$ is the flux of water within the membrane. Water transport within the membrane is due to two separate mechanisms - diffusion and electro-osmotic drag:

$$J^m_{\mathrm{H_2O}} = -D_m \frac{\partial C^m_{\mathrm{H_2O}}}{\partial z} + \xi \frac{j}{\mathcal{F}} \tag{13}$$

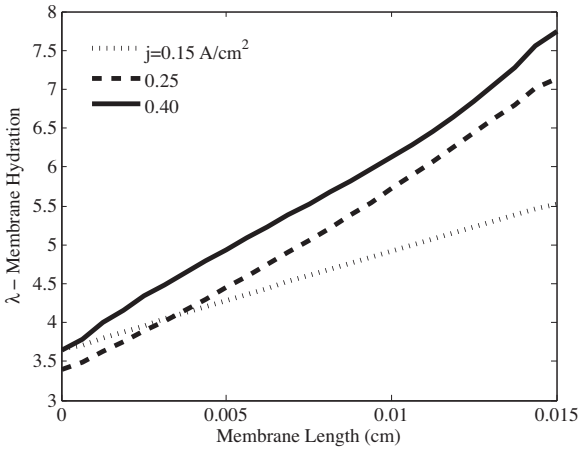

Fig. 3. Typical hydration profiles.

If the diffusion and drag coefficients D_m and ξ are assumed constant, then the following model will arise.

$$\frac{\partial C^m_{H_2O}}{\partial t} = D_m \frac{\partial^2 C^m_{H_2O}}{\partial z^2} \tag{14}$$

$$J^a_{H_2O} + D_m \frac{\partial C^m_{H_2O}}{\partial z} - \frac{j\xi}{\mathcal{F}} = 0 \quad \text{at } z = 0 \tag{15}$$

$$-D_m \frac{\partial C^m_{H_2O}}{\partial z} + \frac{j\xi}{\mathcal{F}} + J^c_{H_2O} + r_{H_2O} = 0 \quad \text{at } z = \tau_m \tag{16}$$

The flux of water entering the membrane from the gas chambers (see Fig. 2) is defined as:

$$J^a_{H_2O} = k^a_{gdl}\left[C^a_{H_2O} - C^a_{H_2O,s}\right] \tag{17}$$

$$J^c_{H_2O} = k^c_{gdl}\left[C^c_{H_2O} - C^c_{H_2O,s}\right] \tag{18}$$

where $C^i_{H_2O,s} = a^i_w P_{vap}(T^s)/RT^s$ and a^i_w satisfies the gas/membrane equilibrium relation at the chamber interfaces.

$$N_s\left(0.043 + 17.81a^a_w - 39.85(a^a_w)^2 + 36.0(a^a_w)^3\right) = C^m_{H_2O}\big|_{z=0} \tag{19}$$

$$N_s\left(0.043 + 17.81a^c_w - 39.85(a^c_w)^2 + 36.0(a^c_w)^3\right) = C^m_{H_2O}\big|_{z=\tau_m} \tag{20}$$

Fig. 3 illustrates typical membrane hydration profiles (Tables 1 and 2), all at steady state and a solid temperature of 80 °C, recall that $\lambda = C^m_{H_2O}/N_s$. At low current density, diffusion dominates and results in a nearly horizontal profile. However, at higher current, the density combined effect of water generation on the cathode side along with electro-osmotic drag, also toward the cathode side, is observed.

3. Solution methodology

The above PEMFC model contains eight Ordinary Differential Equations (ODEs) and one Partial Differential Equation (PDE). While finite element methods could be used to address the PDE portion of the model, an alternative is to approximate the PDE by a set of ODEs. This approach is expected to be of greater utility in future studies aimed at model reduction and the development of a model based controller.

Table 1
Model parameters

Parameter	Description, value, units
$\mathcal{F}$	Faraday's constant, 95485 C mol^{-1}
D^a_{gdl}	Gas diffusion in anode GDL, 0.1490 cm^2 s^{-1}
D^c_{gdl}	Gas diffusion in cathode GDL, 0.0295 cm^2 s^{-1}
D_m	Water diffusion in membrane, 1.5×10^{-6} cm^2 s^{-1}
ξ	Electro-osmotic drag coefficient, 1
N_s	Number of sulfonic sites, 0.00197 mol cm^{-3}
C_{ig}	Ideal gas concentration, 3.45×10^{-5} mol cm^{-3}
ρ_s	Density of solids, 0.35 g cm^{-3}
$\tilde{C}_{p,ig}$	Ideal gas heat capacity, 15 J mol^{-1} K^{-1}
$\tilde{C}_{p,s}$	Solids heat capacity, 0.93 J mol^{-1} K^{-1}
$\Delta H_{f,H_2O}$	Heat of formation of water, −286, 000 J mol^{-1}
n	No. of electrons transferred in reaction, 2
α	Charge transfer coefficient, 0.5
j_o	Exchange current density, 0.01 mA cm^{-2}
E^o	Reversible voltage, 1.2 V
τ_a	Thickness of anode GDL, 0.0350 cm
τ_c	Thickness of cathode GDL, 0.0350 cm
τ_m	Thickness of membrane, 0.0150 cm
V_a	Anode gas volume, 1.25 cm^3
V_c	Cathode gas volume, 1.25 cm^3
V_j	Jacket gas volume, 7.5 cm^3
V_s	Solid volume, 7.5 cm^3
A_m	Membrane area, 25 cm^2
U_a, U_c, U_j	Heat transfer coef (gas–solid), 5.2×10^{-4} J s^{-1} cm^{-2} K^{-1}
U_e	Heat transfer coef (solid-ambient), 5.2×10^{-6} J s^{-1} cm^{-2} K^{-1}

3.1. Spacial discretization

The time dependent nature of the boundary conditions (15) and (16) makes them ill-suited for the following discretization method. As such we convert (14)–(16) into a homogeneous form:

$$\frac{\partial C^m_{H_2O}}{\partial t} = D_m \frac{\partial^2 C^m_{H_2O}}{\partial z^2} + f(t,z) \tag{21}$$

$$\frac{\partial C^m_{H_2O}}{\partial z} = 0 \quad \text{at } z = 0^- \text{ and } z = \tau_m^+ \tag{22}$$

where $f(t,z)$ is selected such that (21) and (22) is equivalent to (14) and (16). Clearly $f(z,t)$ will need to be of the form ([30]):

$$f(t,z) = \delta(z)\tilde{J}_o(t) + \delta(z-\tau_m)\tilde{J}_{\tau_m} \tag{23}$$

Table 2
Nominal operating conditions

Parameters	Description, value, units
$C^a_{H_2,o}$	Inlet hydrogen concentration 1.78×10^{-5} mol cm^{-3}
$C^a_{H_2O,o}$	Inlet water concentration in the anode 1.66×10^{-5} mol cm^{-3}
$C^c_{O_2,o}$	Inlet oxygen concentration 6.72×10^{-6} mol cm^{-3}
$C^c_{H_2O,o}$	Inlet water concentration in the cathode 2.47×10^{-6} mol cm^{-3}
$C^c_{N_2,o}$	Inlet nitrogen concentration 2.53×10^{-5} mol cm^{-3}
T^a_o	Inlet anode temperature 80 °C
T^c_o	Inlet cathode temperature 40 °C
F^a_o	Initial flowrate of anode 2.2 cm^3 s^{-1}
F^c_o	Initial flowrate of cathode 5.8 cm^3 s^{-1}
F^j	Nominal flowrate of the cooling jacket 95.9 cm^3 s^{-1}

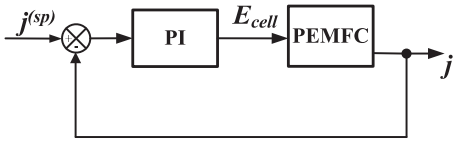

Fig. 4. Current controller configuration.

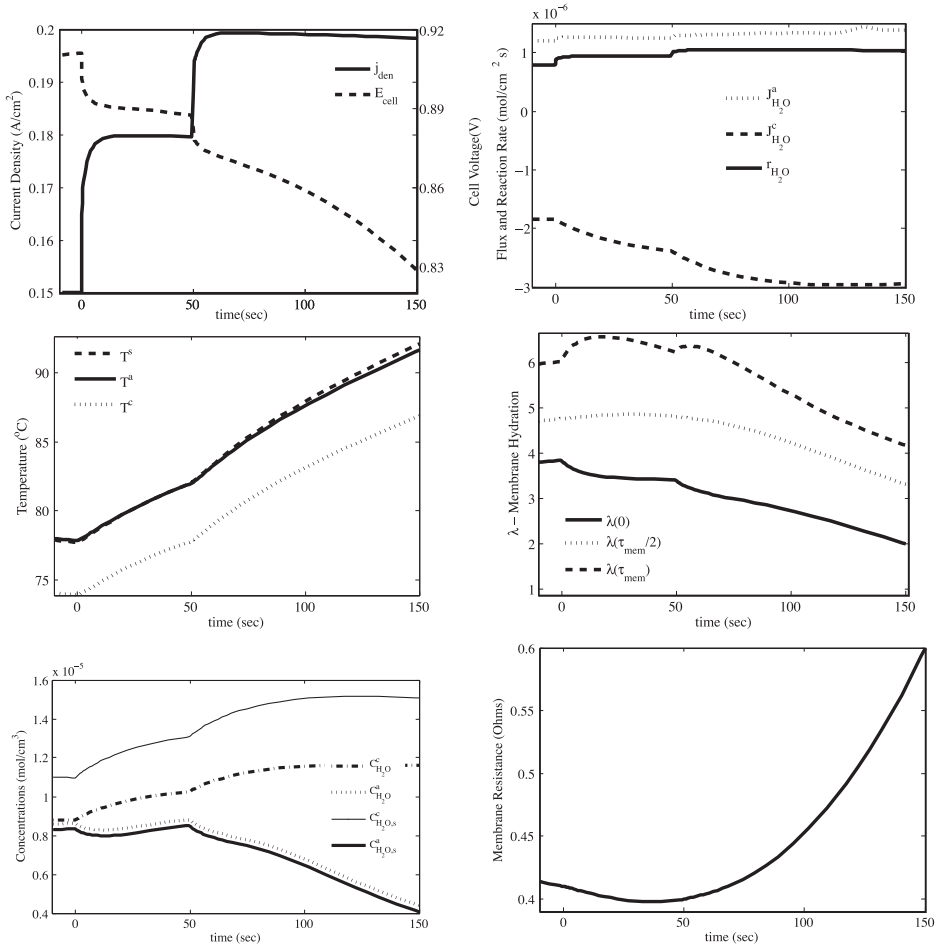

Fig. 5. Simulation of current controller.

where $\delta(\cdot)$ is the Dirac delta function and $\tilde{J}_o, \tilde{J}_{\tau_m}$ are determined by integrating (21) from $z = 0^-$ to 0^+ and $z = \tau_m^-$ to τ_m^+, which yields:

$$\tilde{J}_o(t) = \left[J^a_{H_2O} - \frac{j\xi}{\mathcal{F}} \right] \tag{24}$$

$$\tilde{J}_{\tau_m}(t) = \left[J^c_{H_2O} + \frac{j\xi}{\mathcal{F}} + \frac{j}{n\mathcal{F}} \right] \tag{25}$$

Next, the system (21) and (22) is spacially discretized using the standard Galerkin approach [31]. Let $C^m_{H_2O}(t,z)$ be approximated as follows

$$C^m_{H_2O}(t,z) \simeq C^m_{H_2O,N}(t,z) = \sum_{j=1}^{N} m_j(t)\rho_j(z) \tag{26}$$

where $\rho_j(z) = H_j \cos(w_j z)$ is a sequence of basis functions ($w_j = \pi(j-1)/\tau_m$, $H_j = 1/\sqrt{\tau_m}$ if $j = 1$ and $H_j = 1/\sqrt{(\tau_m/2)}$ otherwise). As the eigenfunction of (21), these are known to be orthonormal under the inner product

$$\langle \rho_i, \rho_j \rangle = \int_0^{\tau_m} \rho_i(z)\rho_j(z)dz \tag{27}$$

Now define a residual function

$$R_N = -\frac{\partial C^m_{H_2O,N}}{\partial t} + D_m \frac{\partial^2 C^m_{H_2O,N}}{\partial z^2} + f(t,z) \tag{28}$$

and enforce the conditions $\langle R_N, \rho_i \rangle = 0, i = 1, \ldots, N$. This results in the following set of ODEs, which will be used to approximate $C^m_{H_2O}(t,z)$ with the help of Eq. (26).

$$\frac{dm_i}{dt} = -D_m w_i^2 m_i + \rho_i(0)\tilde{J}_o(t) + \rho_i(\tau_m)\tilde{J}_{\tau_m}(t) \quad i = 1, \ldots, N \tag{29}$$

3.2. Model structure

The proposed PEMFC model contains $8 + N$ ODEs (Eqs. (1)–(3), (5)–(7), (9), (10), and (29)) along with a number of algebraic relations. In most cases, these algebraic relations are simple functions of the state variables:

$$x = [C^a_{H_2} \quad C^a_{H_2O} \quad T^a \quad C^c_{O_2} \quad C^c_{H_2O} \quad T^c \quad T^j \quad T^s \quad m_i]^T \tag{30}$$

or the manipulated variables

$$u = [F^a_o \quad F^c_o \quad F_j \quad E_{cell}]^T \tag{31}$$

and can be directly substituted into the differential equations. However algebraic relations (11), (19) and (20) are such that an analytic expression for the current density, j, and the membrane surface activities, a^c_w and a^c_w, are not easily obtained. For these three relations, a bisection search algorithm is employed at each time-step of the numeric integration scheme. In sum, the PEMFC model has the following differential algebraic form:

$$\begin{aligned} \frac{dx}{dt} &= f(x,y,u) \\ 0 &= h(x,y,u) \end{aligned} \tag{32}$$

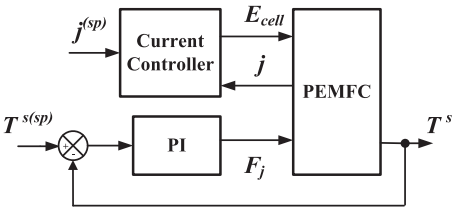

Fig. 6. Current/temperature controller configuration.

where $z = [j \quad a_w^a \quad a_w^c]^T$ and the function $h(x, z, u)$ contains Eqs. (11), (19) and (20).

4. Closed-loop dynamics of membrane hydration

Given the above model, we can now proceed to analyze the dynamic behavior of the membrane. This section will start with a very simple control-loop structure and progressively add complexity. The purpose of this progression is to illustrate the coupling between of the various phenomena within the fuel cell and how these are impacted by the various levels within the final control loop structure.

4.1. Current control

Under this scenario the only form of regulation will be with respect to current, which is manipulated by changes in the cell (or load) voltage. The configuration of Fig. 4 is typical of the electronic load frequently used in experimental studies. As such, we have tuned the Proportional-Integral (PI) controller to be fast responding.

The plots of Fig. 5 illustrate the response to step changes in the current density set-point, $j^{(sp)}$. As indicated by the electrochemistry, a decrease in cell voltage is required to realize the desired increase in current. The increase in current density (and thus power output) will increase the heat production rate, Q_{gen}, as observed in the temperature plot of Fig. 5. The rise in solid temperature will dramatically impact the water concentration at the membrane interfaces, $C^c_{H_2O,s}$ and $C^a_{H_2O,s}$, due to their strong dependence on vapor pressure.

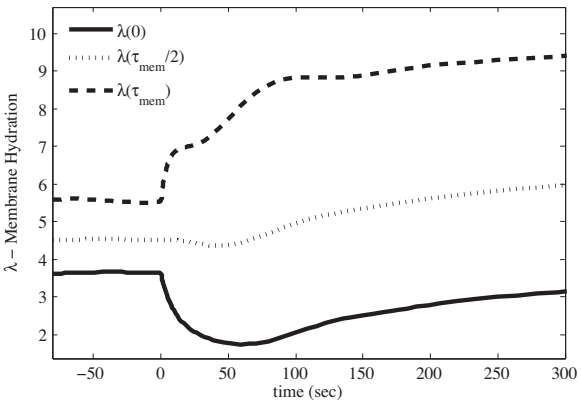

Fig. 8. Expanded view of Fig. 7.

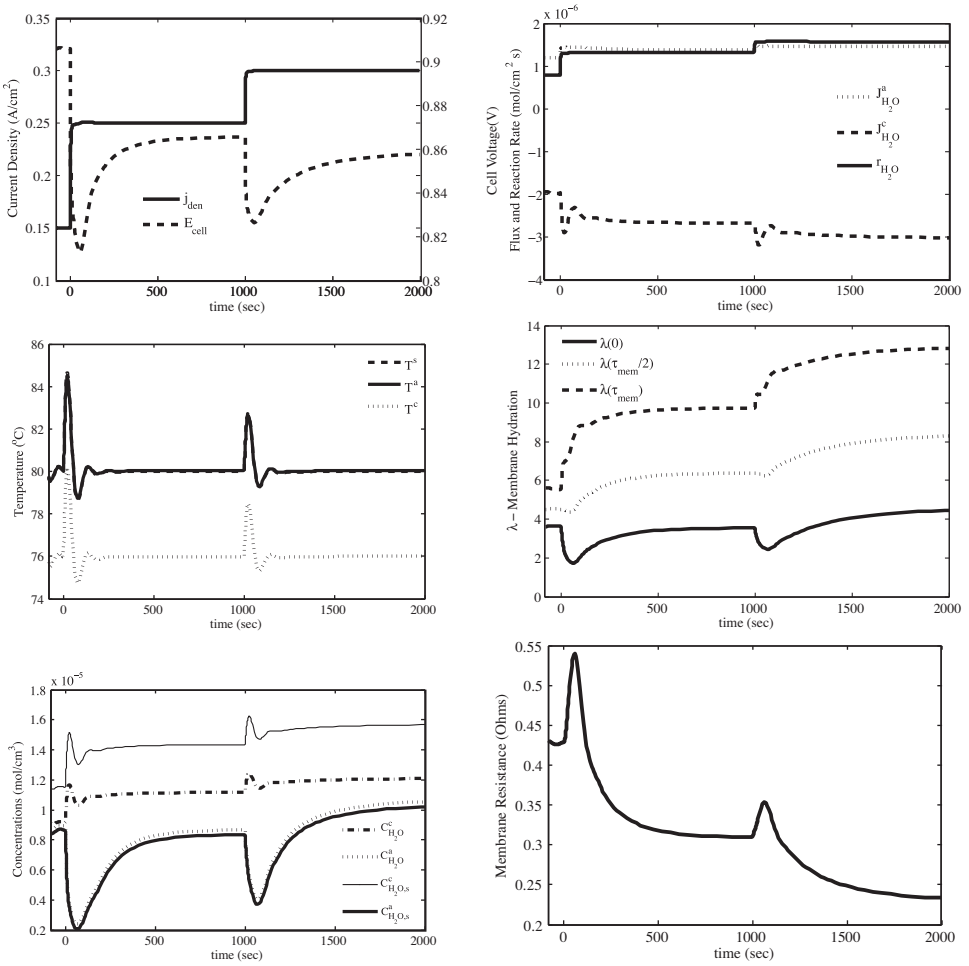

Fig. 7. Simulation of current/temperature controller.

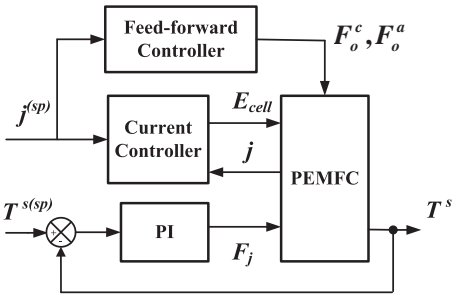

Fig. 9. Feed-forward controller configuration.

This change in surface concentration will increase the flux of water from the membrane to the cathode gas chamber. This is in contrast to the anode side, where the low flow rate through the anode chamber causes the moisture content of the anode gas to track the surface concentration and results in a nearly uniform flux from the anode gas. The net result is an eventual drying out of the membrane. The impact of increased water production and electro-osmotic drag can be seen just after each step change. This is observed as a quick rise in water content at the cathode interface, $\lambda(\tau_m)$, as well as a smaller drop at the anode, $\lambda(0)$. The eventual drying of the membrane causes its resistance to increase, which the current controller compensates for by dropping cell voltage. However, toward the end of the of the simulation the decrease is such that desired current density cannot be maintained.

This first simulation clearly indicates a need for temperature control. Although temperature control is expected to be part of any fuel cell installation, such a controller is likely only able to regulate the bulk (or average) temperature of the stack. Given the spacial nature of an actual fuel cell stack, one would expect the existence of local hot-spots. While the current model cannot capture these spacial aspects, the above simulation suggests the type of phenomena that are likely occurring at the hot-spots.

4.2. Temperature control

We now consider the configuration of Fig. 6. Under this scenario, the temperature of the solid is regulated by manipulation of the cooling jacket flow. Similar to the previous simulation, a change in set-point current density is tracked by decreasing cell voltage. The increase in power output, again, result in an increase in heat production. However, the temperature controller responds by increasing jacket flow which brings the cell temperature back to the set-point (80 °C) in about 200 s. Thus, the flux of water from the cathode undergoes a much smaller increase. This coupled with a larger increase in water production (due to a larger change in set-point current density) results in an eventual increase in membrane hydration (Fig. 7). This will drop ionic resistance and allow the current controller to achieve its set-point at a higher voltage. Again the electro-osmotic drag is observed at the step changes. At the anode interface, $\lambda(0)$, there is a sudden drop in hydration, which even-

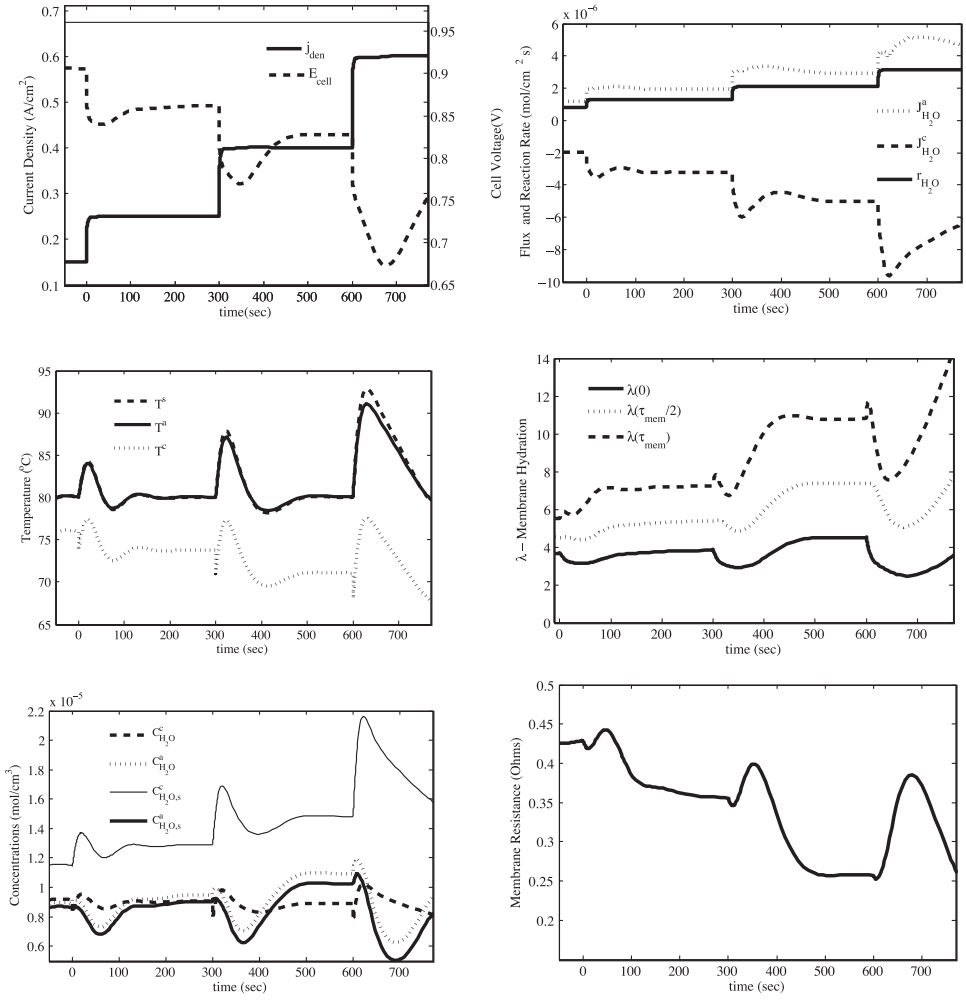

Fig. 10. Simulation with feedforward controller.

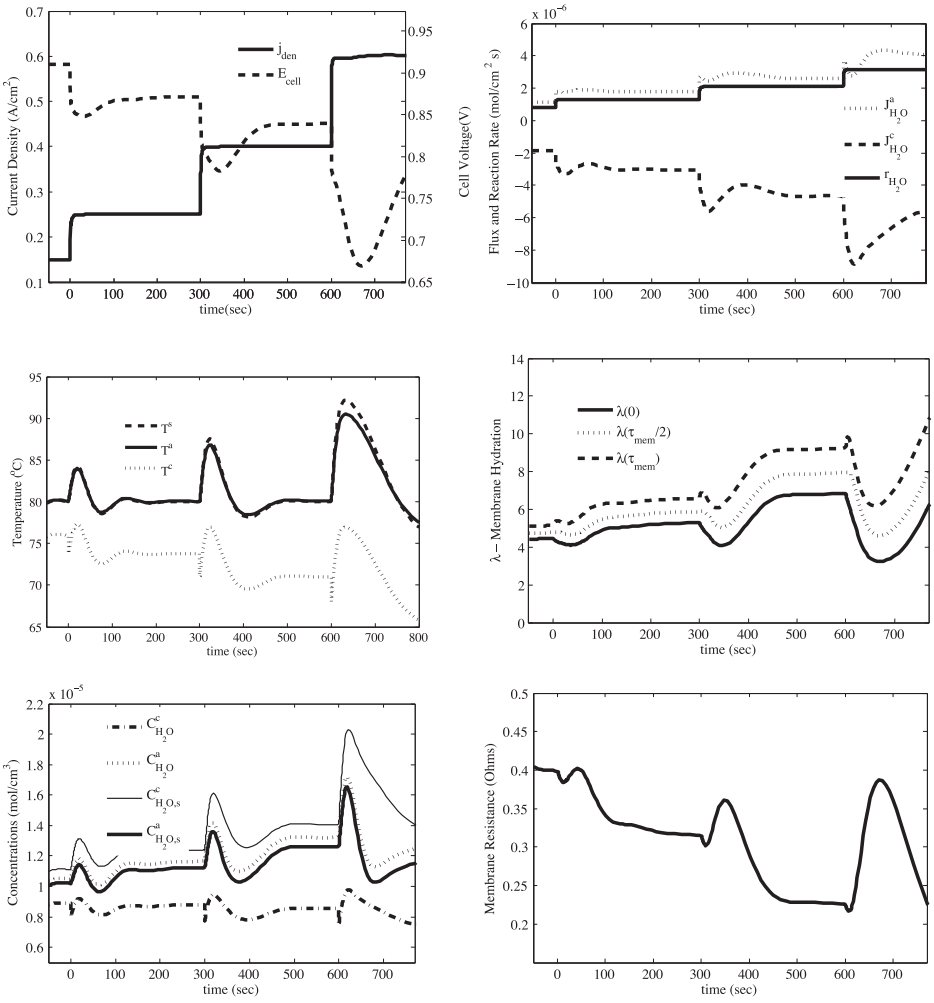

Fig. 11. Simulation with feedforward controller and $D_m = 5 \times 10^{-6}$ cm^2 s^{-1}.

tually comes back due to the overall increase in hydration level. At the cathode interface, $\lambda(\tau_m)$, we see more structure (see Fig. 8). First there is a sudden increase, due to the change in current density and thus electro-osmotic drag. Then the profile appears to level off, due to an increase in water flux to the cathode gas. However, as the temperature controller kicks in, the flux is brought back down and the hydration level again increases, which again increases flux until the two reach a new equilibrium.

4.3. Flow control

In the previous two simulations, the flow of reactant gases to the anode and cathode gas chambers remained unchanged throughout. This, however, is an atypical mode of operation. The more common approach is to vary these flowrates based on a fixed reaction stoichiometry. This scheme is illustrated by the feedforward configuration of Fig. 9. Specifically, the inlet flows are set such that $F_o^a = 2 * j^{(sp)} A_{mem}/n\mathcal{F}C^a_{H_2,o} = 5j^{(sp)}\text{cm}^3\,\text{s}^{-3}$ and $F_o^c = 2 * j^{(sp)} A_{mem}/n\mathcal{F}C^c_{O_2,o} = 40j^{(sp)}\text{cm}^3\,\text{s}^{-3}$. Fig. 10 illustrates operation under this scenario. The impact of the feedforward action is observed at the step change times, where a sharp drop in anode gas temperature and water concentration occurs. Within the membrane the water concentration at the anode interface, $\lambda(0)$, again begins to rise, due to electro-osmotic drag and increased water production. But then, similar to the previous case, this rise is cut short by the increase in water flux from the membrane due to the rise in solid temperature. However, in contrast to the previous case, the flux rise is greater due to the drop in water concentration in the anode gas and results in a slight dip in membrane hydration at the anode interface, just before the eventual rise to the new steady state. While this inverse response is quite small at the time of the first step change it is much more pronounced at the second and especially the third. It is also noted that the drop in anode gas water concentration results in lower hydration levels at steady-state.

5. Discussion

5.1. Membrane flooding

The last two simulations (Figs. 7 and 10) also illustrate an approach to the flooding condition. Specifically, the membrane hydration level at the cathode, $\lambda(\tau_{mem})$, approaches the critical level of $\lambda = 14$. According to Eq. (20), such a value of λ will result in a water activity in the membrane of Fig. 1 and cause the partial pressure of water at the surface to be equal the vapor pressure. The net result is a saturation in the water removal rate in the form of vapor. This suggests that the only mechanism to increase the rate of water removal is in the form of liquid. It should additionally be noted that $\lambda \leq 14$ does not preclude the existence of a liquid water flux. Unfortunately, the literature suggests that there is no agreed upon mechanism describing the flux of liquid water from the membrane. As such the current model makes no attempt to capture the flood-

ing phenomenon. We should also note that temperature gradients in the GDL (specifically a cooling near the GDL/gas chamber interface) could cause water vapor to condense. Again, the current model makes no attempt to capture this phenomenon. However, this condensation scenario does point to a chain of events that would lead to flooding within the spacially dependent realm of an actual fuel cell. If for some reason a cold spot were to occur and cause vapor condensation locally, then the mass transfer of the oxygen reactant would also be reduced locally. This reduction in reaction rate would cause a local drop in heat production and thus further local cooling. This positive feedback would continue until the liquid water grows to a droplet (and eventually a slug) and is moved away by the hydrodynamics of the flowing gases. While the current model cannot capture this chain of events, the above discussion does point to the set of conditions that would lead to flooding, and suggests the future development of a predictive type controller intended to avoid these conditions during operation.

5.2. Impact of diffusion in membrane

The diffusion coefficient of water within the membrane, D_m, plays an important role in the above model. In the previous simulations we used the D_m value suggested by O'Hayre et al. [1] $1.5 \times 10^{-6}\,\mathrm{cm^2\,s^{-1}}$. However, the literature [32] suggests a lack of agreement on the value of this parameter. To illustrate sensitivity with respect to D_m, the simulation of Fig. 10 was repeated (Fig. 11) using a different value for D_m, $5 \times 10^{-6}\,\mathrm{cm^2\,s^{-1}}$. The curves of the second simulation have nearly identical structure to those of the original simulation. Furthermore, with the exception of membrane and anode chamber water concentration, the plot values are about the same. The main difference between the two is the slope of the hydration profile in the membrane, where a greater diffusion flux serves to flatten the profile. With regard to cathode side flooding, this is a positive outcome. On the anode side, the resulting increase in membrane hydration serves to reduce the flux of water from the anode gas chamber, which is observed as an increase in water in the anode gas chamber. While a similar consequence should be observed in the cathode chamber (especially due to the drop in membrane hydration at the cathode interface), the impact is much less pronounced, due to the larger volumetric flowrate through the cathode gas chamber.

6. Conclusions

In this work a PEMFC model featuring an accumulation based through the plane membrane characterization was combined with a variety closed-loop control structures. The simulations presented illustrate a complex set of possible responses, owing to the interaction of multiple phenomena (electro-chemical, chemical, thermal, and membrane hydration) occurring at multiple time-scales. The addition of regulatory and feedforward control loops was shown to have a significant impact on response structure and settling-time, and as such should be included in the dynamic characterization of the PEMFC. It was also noted that changes in membrane diffusivity had a significant impact on water accumulation levels within the membrane.

Acknowledgements

This work was supported by the Department of Chemical and Biological Engineering and the Graduate College at the Illinois Institute of Technology.

References

[1] R. O'Hayre, Fuel Cell Fundamentals, John Wiley & Sons, 2006.
[2] C. Wang, Chemical Reviews 104 (10) (2004) 4727–4766.
[3] S. Paddison, K. Promislow, Device and Materials Modeling in PEM Fuel Cells, Topics in Applied Physics, Springer, 2009.
[4] A. Weber, J. Newman, Chemical Reviews 104 (10) (2004) 4679–4726.
[5] T. Springer, T. Zawodzinski, S. Gottesfeld, Journal of the Electrochemical Society 138 (8) (1991) 2334–2342.
[6] D. Bernardi, M. Verbrugge, Journal of the Electrochemical Society 139 (1992) 2477.
[7] M. Eikerling, Y. Kharkats, A. Kornyshev, Y. Volfkovich, Journal of the Electrochemical Society 145 (1998) 2684.
[8] J. Baschuk, X. Li, Journal of Power Sources 86 (1–2) (2000) 181–196.
[9] T. Nguyen, R. White, Journal of the Electrochemical Society 140 (1993) 2178.
[10] J. Yi, T. Nguyen, Journal of the Electrochemical Society 145 (1998) 1149.
[11] A. Rowe, X. Li, Journal of Power Sources 102 (1–2) (2001) 82–96.
[12] J. Wu, Q. Liu, H. Fang, Journal of Power Sources 156 (2) (2006) 388–399.
[13] B. Zhou, W. Huang, Y. Zong, A. Sobiesiak, Journal of Power Sources 155 (2) (2006) 190–202.
[14] L. You, H. Liu, Journal of Power Sources 155 (2) (2006) 219–230.
[15] J. Pukrushpan, H. Peng, A. Stefanopoulou, Journal of Dynamic Systems, Measurement, and Control 126 (2004) 14.
[16] K. Lauzze, D. Chmielewski, Industrial and Engineering Chemistry Research Fundamentals 45 (13) (2006) 4661–4670.
[17] L. Zhang, M. Pan, S. Quan, Journal of Power Sources 180 (1) (2008) 322–329.
[18] J. Golbert, D. Lewin, Journal of Power Sources 135 (1–2) (2004) 135–151.
[19] J. Golbert, D. Lewin, Journal of Power Sources 173 (1) (2007) 298–309.
[20] R. Methekar, V. Prasad, R. Gudi, Journal of Power Sources 165 (1) (2007) 152–170.
[21] M. De Francesco, E. Arato, Journal of Power Sources 108 (1–2) (2002) 41–52.
[22] Y. Shan, S. Choe, Journal of Power Sources 145 (1) (2005) 30–39.
[23] E. Chia, J. Benziger, I. Kevrekidis, AIChE Journal 52 (11) (2006) 3902–3910.
[24] F. Chen, H. Chu, C. Soong, W. Yan, Journal of Power Sources 140 (2) (2005) 243–249.
[25] Y. Wang, C. Wang, Electrochimica Acta 51 (19) (2006) 3924–3933.
[26] S. Um, C. Wang, Journal of Power Sources 156 (2) (2006) 211–223.
[27] R. Bellows, M. Lin, M. Arif, A. Thompson, D. Jacobson, Journal of the Electrochemical Society 146 (1999) 1099.
[28] D. Hussey, D. Jacobson, M. Arif, J. Owejan, J. Gagliardo, T. Trabold, Journal of Power Sources 172 (1) (2007) 225–228.
[29] P. Quan, M.-C. Lai, D.S. Hussey, D.L. Jacobson, A. Kumar, S. Hirano, Journal of Fuel Cell Science and Technology 7 (5) (2010) 051009.
[30] W. Ray, Advanced Process Control, McGraw-Hill Chemical Engineering Series, McGraw-Hill, 1981.
[31] C. Fletcher, Computational Galerkin Methods, Springer Series in Computational Physics, Springer-Verlag, 1984.
[32] S. Motupally, A. Becker, J. Weidner, Journal of the Electrochemical Society 147 (9) (2000) 3171–3177.